applied sciences

MDPI

Article

Magnetostrictive Patch Transducers for the Generation of Acoustic Waves in Concrete

Zachery L. West [1,*], Shazia Khan [2], Saida Alimdjanova [1], Duncan Billson [1], Lee Marston [3], Sadiq Abdullahi [3], Robin Young [4] and Oksana Trushkevych [1]

[1] School of Engineering, University of Warwick, Coventry CV4 7AL, UK; saida.alimdjanova@warwick.ac.uk (S.A.); d.r.billson@warwick.ac.uk (D.B.); o.trushkevych@warwick.ac.uk (O.T.)
[2] Department of Physics, University of Warwick, Coventry CV4 7AL, UK; shazia.khan@warwick.ac.uk
[3] Fibre Technology Ltd., Brookhill Road, Pinxton, Nottingham NG16 6NT, UK; lee.marston@fibretech.com (L.M.); sadiq.abdullahi@fibretech.com (S.A.)
[4] Lateral Logic Ltd., Yarborough Road, Lincoln LN1 1HP, UK
* Correspondence: zachery.west@warwick.ac.uk; Tel.: +44-7825629007

Featured Application

Magnetostrictive patch transducers were found to provide a convenient, low-cost way to measure local properties of fibre-reinforced concrete non-destructively. This is promising for in-situ quality assurance post production as well as for structural health monitoring where patches or sensor systems can be permanently installed to monitor particular areas prone to stress.

Abstract

Magnetostrictive patch transducers (MPTs) are highly efficient for generating and detecting ultrasonic waves for non-destructive evaluation (NDE), though their use on cementitious media and fibre-reinforced concrete has not yet been investigated. In this study, a COMSOL simulation, validated with laser-Doppler vibrometry, was first used to quantify patch deformation for use in subsequent simulation of wave propagation in samples. The MPT system was then validated on thin glass plates, producing tunable A_0, S_0, and SH_0 modes through frequency-wavelength matching. In cementitious mortar plates, SH_0 and SH_1 modes were demonstrated experimentally for the first time using MPTs. The validated COMSOL model was then used to interpret complex signals in quasi-plate and half-space cementitious mortar prisms, showing that MPTs generate Rayleigh, bulk SH, and surface-skimming SH modes. In steel fibre-reinforced concrete, surface-skimming SH wave speed correlated with increases in breaking strength even in the presence of surface features such as notches. Notably, Rayleigh wave speeds could not be measured in the presence of surface features, and the Rayleigh velocities measured in the same sample, but not in the local tested area did not correlate with SH speed. This behaviour is likely due to the non-uniform distribution of material constituents, including fibre-reinforcement and coarse aggregate, combined with the different propagation paths and depth sensitivities of the reported wave modes. Overall, racetrack-coil MPTs enable multimodal inspection of cementitious media, providing information on the presence of geometric features and material properties.

Keywords: magnetostrictive patch transducers; ultrasonics; non-destructive evaluation; finite element analysis; cementitious media; fibre-reinforced concrete; shear-horizontal; Rayleigh

Check for updates

Academic Editor: Michele D'Amato

Received: 13 May 2026
Revised: 12 June 2026
Accepted: 17 June 2026
Published: 23 June 2026

Copyright: © 2026 by the authors. Licensee MDPI, Basel, Switzerland. This article is an open access article distributed under the terms and conditions of the Creative Commons Attribution (CC BY) license.

1. Introduction

Magnetostrictive patch transducers (MPTs) are a promising ultrasonic transducer technology for non-destructive evaluation (NDE) and structural health monitoring (SHM) particularly where removable attachment, geometric adaptability, and guided-wave control are required. Unlike conventional piezoelectric probes, whose source behaviour is largely governed by the piezoelectric element and contact interface, MPTs use a magnetostrictive patch as an intermediate mechanical source. As a result, the generated wavefield can be influenced by patch geometry, magnetic biassing, coil configuration, excitation frequency, and coupling condition [1–3]. This makes MPTs particularly interesting for applications requiring mode control, source directionality, or adaptation to complex geometries. However, while MPTs have been widely studied in metallic plates and pipes, their behaviour in thicker heterogeneous materials such as concrete remains under-explored.

MPTs generate forces through the Joule and Wiedemann effects [4] through a combination of static biassing and pulsed magnetic fields. The pulsed magnetic field is obtained by pulsing current through a coil of wire, while the bias field is generated by permanent magnets. This bias is necessary because magnetostriction varies nonlinearly with magnetic field [5], and biassing the magnetic field brings the operation within a region of maximum slope where small changes in field induce the largest strain response [3]. MPTs also convert strain into magnetic field which is picked up as current in a coil above the patch through the Villari (inverse Joule effect) and Matteucci effect (inverse Wiedemann effect).

Recent MPT research has progressed from basic guided-wave generation towards transducers with improved mode control, directionality, array operation, and signal strength. Kim and Kwon [2] reviewed MPT applications in ultrasonic NDE of waveguides prior to 2015, while Vinogradov et al. [6] discussed new MPT designs for emerging NDE applications. For SH-wave generation, Wang et al. [1] developed a unidirectional wideband SH guided-wave phased-array MPT, and Liu et al. [7] demonstrated direction-tunable SH-mode generation using an array MPT. Beam focusing and directional control have also been investigated using circular and anisotropic patch configurations [8,9]. In parallel, magnetic biassing and magnetic-circuit optimisation have been shown to influence MPT performance and signal strength [10,11], while removable and flexible patch designs have expanded the practical deployment possibilities of MPTs [12,13]. Finite-element and equivalent-source models have also been developed to relate patch actuation to the elastic field generated in a structure [3,14–16]. MPTs have also been applied extensively to pipe inspection, including torsional and longitudinal guided-wave configurations, where patch geometry can be adapted to curved metallic surfaces [17–19]. These studies show that MPTs are not only convenient alternatives to conventional probes, but increasingly tuneable ultrasonic sources whose wavefield can be modified through transducer design.

A key reason MPTs are relevant to this study is their ability to generate several ultrasonic wave components from a single patch-based source. Previous work has shown that MPTs can generate SH, S_0, and A_0 guided-wave modes, with relative modal amplitudes and directivity affected by patch geometry, excitation frequency, and magnetic field distribution [13,20]. SH-wave transducers are attractive for NDE and SHM because they generate in-plane shear motion, with the fundamental SH_0 mode offering near non-dispersive propagation in plate-like structures. However, efficient and selective SH-wave generation often requires transducer designs specifically suited to shear motion, including shear-mode piezoelectric transducers, electromagnetic acoustic transducers, or MPTs [21]. This makes MPTs attractive where in-plane shear excitation, modal tuning, and removable attachment are required.

Concrete is a ubiquitous material in modern engineering structures. However, long-term loading, environmental exposure, construction defects, and material variability can

lead to cracks, voids, stiffness changes, and other forms of internal damage, reducing structural integrity and durability [22,23]. In concrete, where surface condition, scattering, attenuation, and local heterogeneity strongly affect ultrasonic measurements, a tuneable patch-based source provides a route to generating and comparing multiple wave components, including SH, Rayleigh-type surface responses, SV components, surface-skimming waves, and bulk responses.

Ultrasonic testing remains a crucial tool for concrete NDE [23]. It can support visualisation of internal defects, stress evaluation, and quantitative assessment of damage in concrete structures [24–27]. Recent advances in nonlinear acoustics have improved sensitivity to early micro-damage compared with velocity measurements alone [25], while multiple-scattering models have improved interpretation of attenuation and velocity in heterogeneous concrete mixes [28]. Recent reviews also highlight how improved ultrasonic hardware, combined with connected sensing and data-driven analysis, is supporting new structural health monitoring frameworks for civil infrastructure [29,30].

The successful use of MPTs in metallic waveguides therefore does not directly establish their behaviour in cementitious media. Metallic plates and pipes are comparatively homogeneous, low-attenuation structures with smoother surfaces and more predictable guided-wave behaviour. Conversely, concrete is a heterogeneous cementitious composite with stronger scattering, higher attenuation, rougher contact conditions, and greater local variability. These factors can alter both the coupling of the patch to the surface and the subsequent balance between modal content. Therefore, although MPT-based SH and Lamb wave generation has been widely studied in metallic waveguides, the wavefield characteristics, mode selectivity, and defect-detection mechanisms of MPTs in thick-walled and non-uniform concrete remain unclear.

This paper aims to extend MPT research from established metallic waveguide applications into concrete and other thick heterogeneous structures. The novelty is not the generation of SH or Rayleigh waves by MPTs, but the systematic investigation of how racetrack-coil MPT deformation produces multimodal ultrasonic wavefields in cementitious media, and how these wavefields can be interpreted for defect detection and material-property assessment. To achieve this, patch deformation is first quantified using LDV-validated COMSOL (version 6.4) modelling before mode generation is validated in a thin glass plate. The approach is then extended to cementitious mortar plates and prisms to identify SH, Rayleigh/SV, bulk, surface-skimming, and reflected wave components across different thickness-to-wavelength regimes. Finally, the usefulness of these multimodal responses is examined using defected cementitious mortar blocks and steel fibre-reinforced concrete specimens. This provides a foundation for using MPTs not only as practical ultrasonic sources, but as tuneable multimodal transducers for concrete NDE and structural health monitoring.

2. Materials and Methods

Throughout this paper, we use the following notation: X is in-plane (SH) motion, Z is out-of-plane motion, and Y is the direction of propagation. This work investigates ultrasonic behaviour spanning across multiple thickness-to-wavelength (d/λ) regimes, generically described in Table 1, with representative dispersion curves shown in Figure 1.

Ultrasonic waves can propagate in several distinct modes, each distinguished by its own particle-motion pattern and propagation velocity. For added context Table 2 details common wave modes, speeds, and dominant components.

Table 1. Regimes for elastic-wave propagation in media as a function of the thickness-to-wavelength (d/λ) ratio. Cut-offs are approximate and follow the half-space/plate guidance in [31].

Thickness/Wavelength Ratio (d/λ)	Propagation Regime	Dominant Wave Modes
>10	Half-space	Bulk Longitudinal (P), Bulk Shear (SV/SH), Rayleigh (Surface)
≈3–10	Quasi-plate	Mixed bulk/guided behaviour, SH_n, higher-order Lamb modes (S_n, A_n) with Rayleigh beginning to dominate.
≤3	True plate	Fully guided plate modes: Lamb (S_0, A_0, S_n, A_n) and Shear Horizontal (SH_0, SH_n)

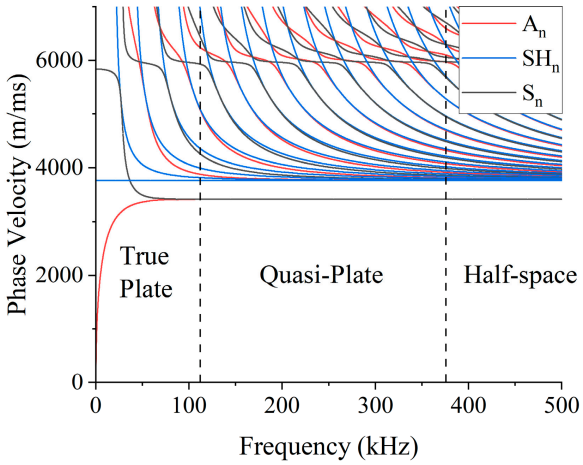


Figure 1. Dispersion curve of 100 mm thick glass showing asymmetric (A_n), symmetric (S_n), and shear-horizontal modes (SH_n) up to 500 kHz. Regimes are calculated from SH_0 speed and follow d/λ expressions in Table 1. Dispersion curves are computed using the open-source dispersion calculator by Armin Huber (https://github.com/ArminHuber/Dispersion-Calculator, accessed 10 February 2026).

Table 2. Ultrasonic wave types in isotropic elastic solids, showing velocity expressions and key inspection attributes relevant to non-destructive evaluation [31,32]. Symbols: c wave speed; λ wavelength; K bulk modulus; G shear modulus; ρ density; ν Poisson's ratio; d plate thickness with $h = d/2$; f frequency with $\omega = 2\pi f$; k in-plane wavenumber; $v_p = \omega/k$ phase velocity; n mode order; $f_{c,n}$ cutoff frequency of the nth SH mode; $c_{p,n}$ phase velocity of nth SH mode; c_L bulk longitudinal wave speed; c_S bulk shear wave speed; c_R Rayleigh wave speed; α and β Rayleigh–Lamb thickness wavenumbers defined by $\alpha^2 = \omega^2/c_L^2 - k^2$ and $\beta^2 = \omega^2/c_S^2 - k^2$.

Wave Type	Velocity/Key Relations	Description (NDT Relevance)
Longitudinal bulk (P)	$c_L = \sqrt{\frac{K+\frac{4}{3}G}{\rho}}$	Fastest bulk wave, strongest through-transmission in many solids, good for volumetric inspection.
Shear bulk: (SH/SV)	$c_s = \sqrt{\frac{G}{\rho}}$ $(typ.\ c_s \approx 0.5 - 0.6\ c_L)$	Bulk shear with particle motion perpendicular to propagation. SV: motion is out-of-plane. SH: motion is in-plane. Sensitive to cracks depending on orientation relative to particle motion.

Table 2. *Cont.*

Wave Type	Velocity/Key Relations	Description (NDT Relevance)
Rayleigh surface	$c_R \approx \frac{0.862+1.14\nu}{1+\nu} c_s$ $\left(typ.\ 0.87 < \frac{c_R}{c_s} < 0.96\right)$	Surface-confined (decays with depth), retrograde elliptical motion. Strong sensitivity to true surface and near-surface defects.
SH plate modes (SH_n)	$c_{SH_0} = c_s$ $f_{c,n} = \frac{nc_s}{2d},\ n \in \mathbb{N}, n \geq 1$ $c_{p,n} = \frac{c_s}{\sqrt{1-(f_{c,n}/f)^2}}$	Guided-wave family derived from bulk SH, particle motion in-plane and perpendicular to propagation. Higher orders are dispersive and depend on frequency-thickness product. SH_0 is simplest for interpretation/long range testing while being non-dispersive.
Lamb plate modes (S_n, A_n)	$(S):\ \frac{\tan(\beta h)}{\tan(\alpha h)} = -\frac{4\alpha\beta k^2}{(k^2-\beta^2)^2}$ $(A):\ \frac{\tan(\beta h)}{\tan(\alpha h)} = -\frac{(k^2-\beta^2)^2}{4\alpha\beta k^2}$	Guided waves formed by coupled P and SV fields. Velocities depend on frequency—thickness product (*fd*). Lowest modes (S_0, A_0) enable long-range inspection; dispersive so mode/packet ID matters.

A racetrack-coil MPT was selected for this study. The MPT consisted of a rectangular 0.1 mm thick $Fe_{50}Co_{50}$ patch, and excited by an AC-driven racetrack coil with dual biassing magnets, as illustrated in Figure 2a. The FeCo patch material was a commercially supplied $Fe_{50}Co_{50}$ soft magnetic iron–cobalt–vanadium alloy strip, supplied as Vacoflux 50/ASTM A801 Alloy 1 equivalent coil stock. The material was cut manually to the required rectangular patch geometry using scissors. No additional magnetisation or post-processing treatment was applied to the patch before testing. The patch width (along Y) is selected to correspond with the desired mode wavelength, consistent with findings in [33], while the patch length (along X) is kept around three wavelengths to keep reasonable generation directivity. Racetrack coils are wound with Ø0.2 mm enamelled copper wire, with width and length equal to the patch dimensions, and with a 3 mm gap in the centre. Biassing permanent magnets are Nd:Fe:B of 40 × 10 × 5 (mm^3) size, producing magnetic field of 3 mT in the centre of the patch. This places the $Fe_{50}Co_{50}$ patch within the ideal biassing region as reported in [33]. The racetrack-coil MPT configuration is effective in producing SH modes in plates, Lamb waves can also be produced at the same time due to the patch's non-perfect horizontal motion and twisting effects [2,8,13,34]. Patch mode generation is governed by four key factors: patch shape and dimensions, magnetic field generation, wavelength of the generated modes, and patch coupling.

Unless stated otherwise all ultrasonic experimentation used the same setup. The transmitting racetrack-coil MPT was driven from the high-power output of a Ritec RPR-4000 pulser-receiver, while the received signal was acquired using a Tektronix 2-Series Mixed Signal Oscilloscope at a sampling frequency of 250 MHz. Oscilloscope averaging was applied over twelve repeated acquisitions with triggering provided by the Ritec RPR-4000 pulser-receiver to ensure consistent temporal alignment. Tests were conducted in the Warwick Engineering ultrasonics laboratory under controlled low-noise environmental conditions.

The transmitting and receiving MPTs were attached to the cementitious media surface using Tesa® 4965 double-sided adhesive tape, a thin 0.2 mm PET-backed acrylic tape chosen to provide strong adhesion while minimising the compliant coupling layer between the patch and cementitious media. Tape is widely used for MPT adhesion proving to support low frequency [11], and multimodal generation [13]. For all cementitious media

experimentation, the patch adhesion locations were lightly prepared to remove loose surface sediment to improve contact adhesion and reduce tape sediment saturation, while tape was smoothed to reduce air gaps.

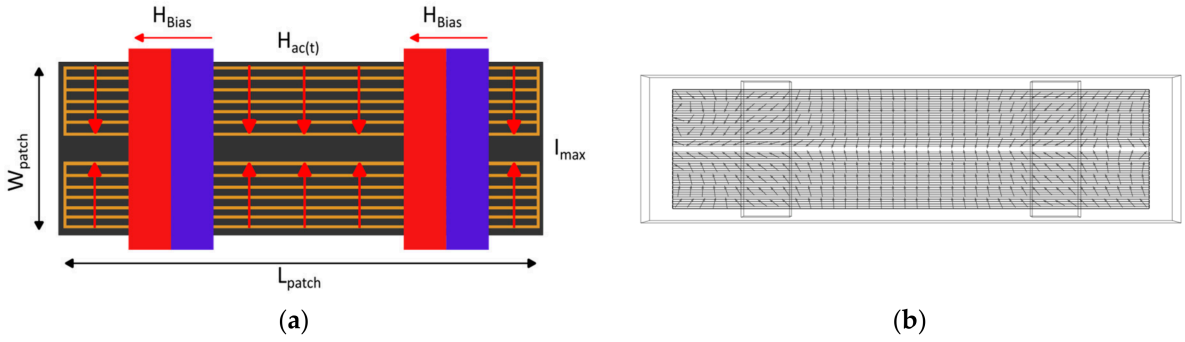


Figure 2. (**a**) A schematic of the racetrack-coil MPT showing bias field H_{Bias}, time-varying excitation field $H_{ac(t)}$, patch dimensions L_{patch} and W_{patch} at maximum input (I_{max}); (**b**) magnetisation profile of racetrack-coil MPT at I_{max} simulated in COMSOL with arrows indicating magnetisation vectors.

In order to analyse the complex ultrasonic signals observed in the experiments, finite element modelling is used. Finite element modelling also aids the challenging task of identifying and visualising wave modes and their propagation. For all simulation components of the ultrasonic experiments presented in this paper, the Solid Mechanics and Elastic Waves modules of COMSOL Multiphysics® (COMSOL AB, Stockholm, Sweden) were utilised.

2.1. Patch Deformation Modelling and Validation

Two methodologies were used to quantify the patch deformation in racetrack-coil MPTs: firstly, laser-Doppler vibrometry (LDV) was used to find the deformation profile of the patches, and then COMSOL was used to generate an equivalent force model for ultrasonic simulation. A methodology was developed to gain in-plane insights, from out-of-plane only vibrometry equipment. By 3D printing $2 \times 2 \times 10$ (mm^3) pins; applying reflective aluminium tape to one side; adhering this to the patch; directing the laser to sense the side of the pin; in-plane components can be measured. Measurements were obtained using a Polytec OFV-505 LDV with the OVR-SR lens. At the approximate 0.4 m working distance, this gives a specified spot diameter of ~121 µm as per manufacturer specifications, which was visibly smaller than the reflective pin area and did not overlap the pin edges. This setup is seen in Figure 3a.

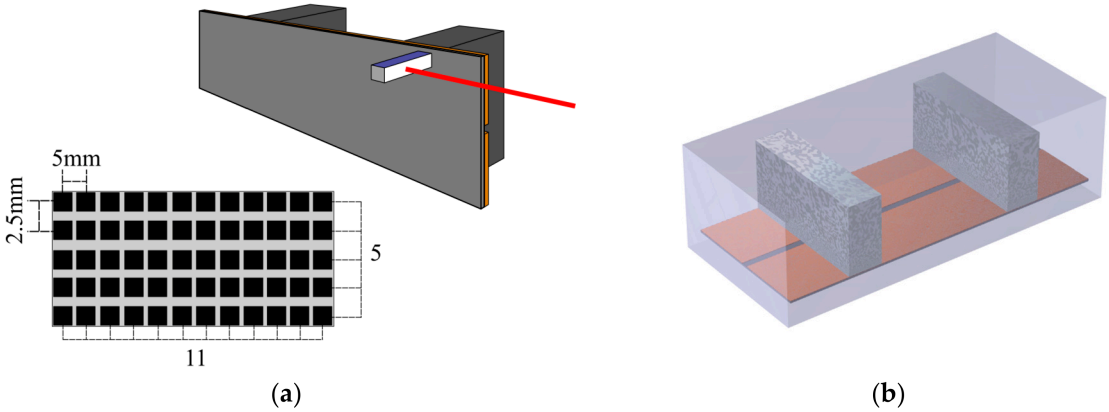


Figure 3. Patch deformation methodology displaying: (**a**) LDV setup used for finding in-plane motion from an out-of-plane LDV and scanning array; (**b**) COMSOL setup for finding patch deformation using COMSOL's non-linear magnetostriction module.

The COMSOL simulation of the magnetostriction present in a racetrack-coil MPT was conducted using the non-linear magnetostriction module, as shown in Figure 3b. To enable comparison between LDV and COMSOL simulation data, point probes were placed at the same spatial locations as the 11 × 5 LDV measurement array, mirroring the layout shown in Figure 3a. The deformation data were then extracted from these probe locations using COMSOL's built-in finite-element solution interpolation and decomposed into the orthogonal displacement components μ_x, μ_y and μ_z.

2.2. Mode Generation

Mode generation experiments were conducted in a 600 × 600 × 3 (mm^3) glass plate using the racetrack-coil MPT configuration. Glass was chosen as the initial test material due to its homogeneity, isotropy, and low acoustic attenuation compared to more complex media such as concrete. By varying the frequency on a single 95 × 20 × 0.1 (mm^3) MPT, observations on mode selectivity for frequency via wavelength can be made. The experiment setup is seen in Figure 4. The glass was supported on bubble wrap to minimise mechanical impedance to the support surface, reducing damping and allowing free vibration. Two 95 × 20 × 0.1 (mm^3) racetrack-coil MPTs were bonded with double sided tape to opposite edges of the glass plate in a pitch–catch configuration. The transmitting racetrack-coil MPT was driven using a 4-cycle tone-burst. The receiving racetrack-coil MPT had gain of 40 dB applied.

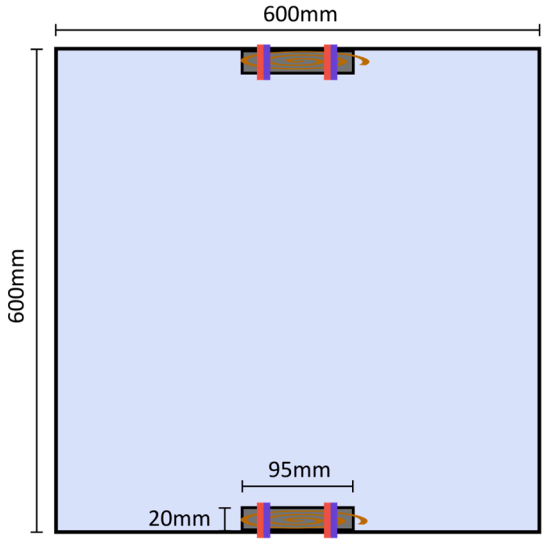


Figure 4. Experimental setup for 600 × 600 × 3 (mm^3) glass pitch-catch using two 95 × 20 × 0.1 (mm^3) MPTs.

2.3. MPTs on Cementitious Mortar Plates

MPT generation, detection and subsequent degeneration of SH-guided waves in 30 mm thick cementitious mortar plate was then investigated, with the wavelength close to dispersion curves of Figure 5b indicate SH cutoffs and phase velocities. Experimentation based on methodology in [35] for higher-order modal validation of SH was conducted on a 30 mm thick cementitious mortar plate, as illustrated in Figure 5a. Here a pulse is generated on transducer t_1 and detected on two sides of the plate by sensors s_1 and s_2. This way, the symmetric SH_0 mode will arrive at s_1 and s_2 at the same time with the same phase, while the antisymmetric SH_1 mode will arrive at these sensors at the same time with opposing phase. The transmitting racetrack-coil MPT was driven at 70 kHz, using a 5-cycle tone-burst; the transmitting patch had dimensions 80 × 30 × 0.1 (mm^3). The receiving MPT had gain of 50 dB applied. The plate was produced from an approximate

2:1 sand-to-cement mixture by volume, with no coarse aggregate, a water-to-cement ratio of approximately 0.5, and was cured for over 30 days before testing.

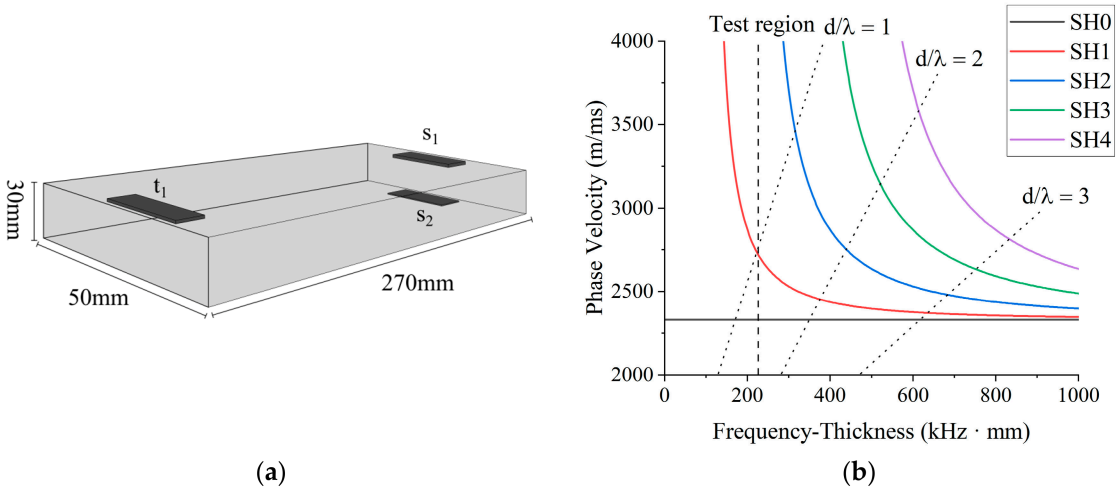


Figure 5. Cementitious mortar plate experimentation showing: (**a**) Illustrated schematic of experiment setup with dimensions and transducer–sensor locations shown; (**b**) Dispersion curve for cementitious mortar with parameters: 30 mm thickness, E = 90 GPa, ρ = 2300 kgm^3, ν = 0.2 calculated from equations in [31]. The dispersion curves were derived under the assumption of a homogeneous elastic medium and should therefore be interpreted as idealised reference solutions for first-order modal interpretation, rather than as direct representations of real coarse-aggregate concrete.

2.4. MPTs on Cementitious Mortar Prisms

Before utilising MPTs on concrete for NDE, an understanding of their generated wavefields in cementitious media is required. To investigate the ultrasonic field generated by racetrack-coil MPTs in a simplified concrete-like material, a study was undertaken on a cementitious mortar prism with dimensions of 100 × 500 × 100 (mm^3), as seen in Figure 6. The prism was produced from an approximate 2:1 sand-to-cement mixture by volume, with no coarse aggregate, a water-to-cement ratio of approximately 0.5, and was cured for over 30 days before testing. Firstly, a COMSOL simulation of the ultrasonic wavefield was performed to confirm and illustrate wave mode packets and visualise orthogonal energy components at 120 kHz input frequency using an equivalent force model created from the patch deformation study, seen in Figure 6a. The external boundaries were modelled as free boundaries to represent the finite specimen geometry, so that edge and surface reflections were retained as they would be in the experimental measurements. While this increases waveform complexity and modal overlap, it avoids artificially suppressing reflections that are physically present in the measured finite-specimen response. Next, a pitch-catch test between an out-of-plane piezoelectric sensor and a racetrack-coil MPT transducer was performed to confirm the polarity of wave packets from a MPT generated wavefield in cementitious media, the sensor was placed 0.4 m from the transducer on the prism, as seen in Figure 6b. The transmitting racetrack-coil MPT was driven at 120 kHz, using a 5-cycle tone-burst, transmitting patch had dimensions 80 × 30 × 0.1 (mm^3). The receiving piezo had a central frequency of 120 kHz and had gain of 60 dB applied. Finally, an experiment was performed using four matched racetrack-coil MPT sensors mounted on the sample with double sided tape: two on the same face at positions 0.205 m (1-2) and 0.330 m (1-3), and two on the opposite face ((1-4)(1-5)), directly below their 1-2 and 1-3 counterparts to identify wave speeds and reflection paths, as seen in Figure 6c. The transmitting racetrack-coil MPT was driven at 230 kHz, using a 5-cycle tone-burst, patches were 60 × 12.5 × 0.1 (mm^3). The receiving MPT had gain of 60 dB applied.

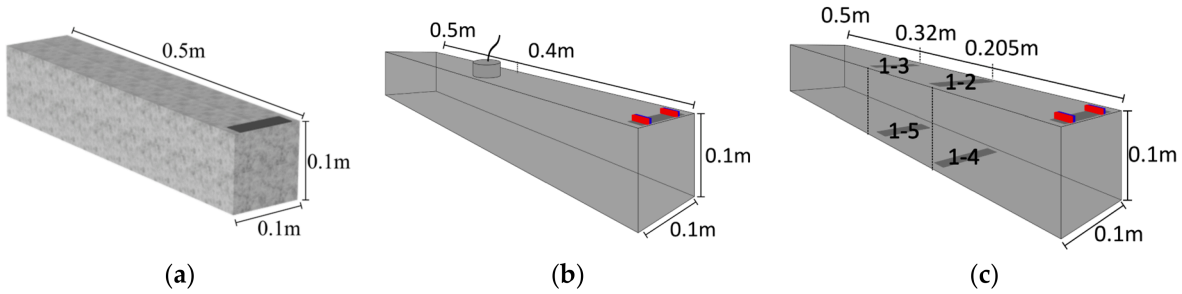


Figure 6. Experimental setup for 100 × 500 × 100 (mm^3) cementitious mortar prism with dimensions and sensor locations, showing: (**a**) COMSOL setup; (**b**) MPT-piezo; (**c**) MPT-MPT with four sensor locations.

2.5. Defect Effects on Wave Propagation in Cementitious Mortar Prisms

To demonstrate the defect sensitivities of the racetrack-coil MPT generated multimodal wavefield, a cementitious mortar block measuring 200 × 320 × 145 (mm^3) and containing two flat-bottom holes (30/70 mm in diameter/depth) was examined, the experimental setup is shown in Figure 7. Two datasets were acquired: (1-1) with the transducer and receiver on the surface containing the defects, and (2-2) with both instruments positioned on the opposite surface. The transmitting racetrack-coil MPT was driven at 190 kHz, using a 5-cycle tone-burst, patches were 80 × 20 × 0.1 (mm^3). The receiving MPT had gain of 60 dB applied. The block was produced from an approximate 2:1 sand-to-cement mixture by volume, with no coarse aggregate, a water-to-cement ratio of approximately 0.5, and was cured for over 30 days before testing.

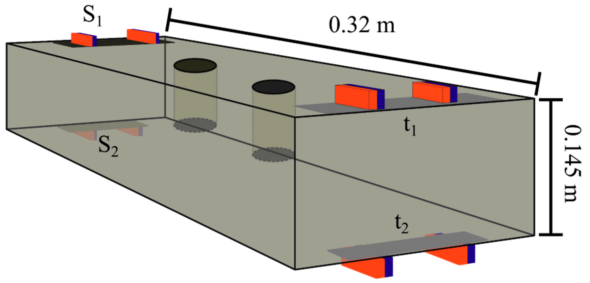


Figure 7. Experiment setup for flat-bottom hole cementitious mortar sample showing transducer–sensor locations for first (1-1) and second dataset (2-2).

2.6. Tests on Fibre-Reinforced Concrete Prisms

Experimentation was performed on fibre-reinforced concrete prisms. A total of five samples of fibre-reinforced concrete with dimensions 150 × 650 × 150 (mm^3) were tested on two faces before and after a 3-point bend test in a hydraulic press, seen in Figure 8a, where the samples were tested until failure. The samples had a notch of dimensions 150 × 5 × 30 (mm^3) cut into one side (Side 1), the samples were nominally identical, although local fibre-reinforcement density around Side 1 was expected to vary. The transmitting racetrack-coil MPT was driven at 80 kHz, using a 4-cycle tone-burst, patches were 95 × 40 × 0.1 (mm^3). The receiving MPT had gain of 60 dB applied. These experiments were performed at BRE facility where nearby large machinery was turned off to reduce electromagnetic interference and noise. The fibre-reinforced concrete prisms were cast using a CEM II/A-LL cement-based mix with Thames Valley aggregates. The constituent quantities were 370 kg/m^3 cement, 564.025 kg/m^3 20–10 mm aggregate, 646.363 kg/m^3 10–4 mm aggregate, 646.363 kg/m^3 4–0 mm aggregate, and 179.949 kg/m^3 tap water. Fibre-reinforcement was provided by Fibrex DS melt-extracted steel fibres with dimensions of 25 × 0.5 mm, added at 71.901 kg/m^3, equivalent to 3% by weight.

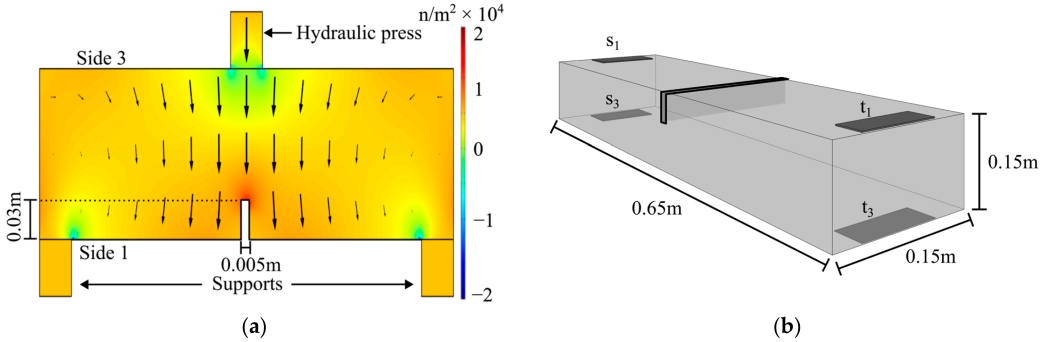


Figure 8. Pre-notched fibre-reinforced concrete prism tests showing: (**a**) three-point bending configuration and corresponding COMSOL simulated stress field. Warmer colours indicate higher stress in the direction associated with fracture, with peak stress localising at the notch region. Arrows indicate applied load and support reactions with notch geometry shown; (**b**) diagram of fibre-reinforced concrete prism showing transducer–sensor locations for Side 1 (t_1-s_1) and Side 3 (t_3-s_3).

3. Results

3.1. Patch Deformation

Figure 9 displays comparisons between μ_x, μ_y and μ_z data at maximum AC input voltage (I_{max}) for both COMSOL simulation and LDV readings. Clear similarities can be observed between LDV and COMSOL X and Y deformation data. Dominant actuation vectors for X and Y are displayed in Figure 9a,b, which are observed to follow magnetisation vectors simulated in Figure 2b. Z-motion Figure 9c,d is less consistent with a larger deformation shape following magnetisation vectors, with multiple ripples across the patch, LDV and COMSOL readings at I_{max} are similar. All I_{min} values were found to mirror I_{max}.

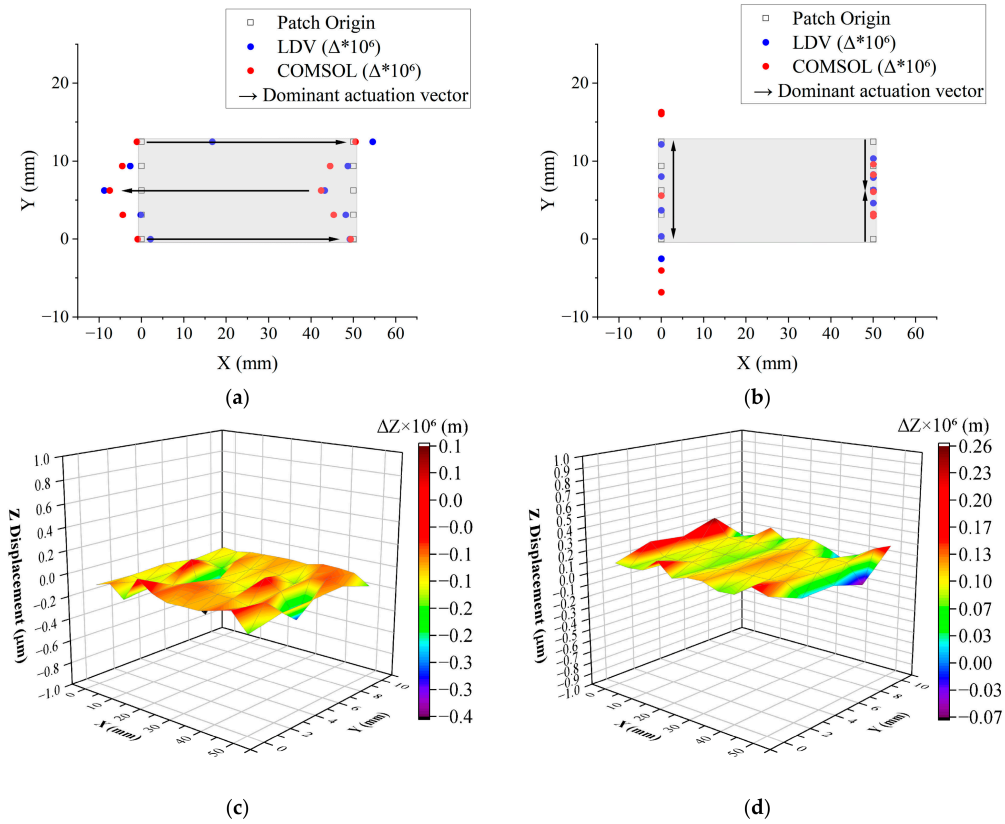


Figure 9. Laser Doppler Vibrometry (LDV) and COMSOL displacement readings for a racetrack-coil MPT at maximum AC input voltage (I_{max}), showing: (**a**) X-displacement for both COMSOL and LDV; (**b**) Y-displacement for COMSOL and LDV; (**c**) Z-displacement for LDV; (**d**) Z-displacement for COMSOL.

3.2. Mode Generation Validation

Figure 10a displays the frequencies of maximum modal excitation, approximately 190 kHz for SH_0 and 140 kHz for A_0 on the setup in Figure 4. After calculating wave speeds from arrival times, we find the SH_0 wavelength to be 19.6 mm and the A_0 wavelength to be 17.8 mm at the most efficient generation frequencies. Figure 10b, plots maximum amplitude as a function of frequency. Clear bell curves can be seen around both modes' most efficient generation.

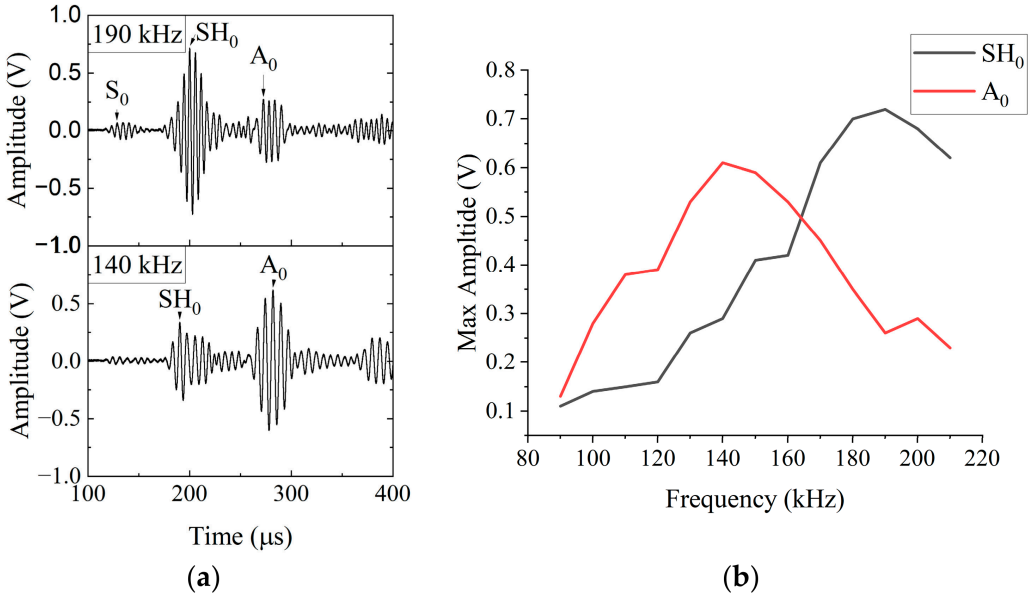


Figure 10. Experimental results from tests on a 3 mm thick glass plate (setup in Figure 4), showing: (**a**) Waveform data for two selected frequencies at which the maximum mode amplitude occurs with the wave packets are assigned to S_0, A_0 and SH_0 wave modes as indicated by arrow labels; (**b**) Frequency vs. maximum amplitude for SH_0 and A_0 modes using a $95 \times 20 \times 0.1$ (mm^3) MPT.

3.3. MPTs Results on Cementitious Mortar Plates

Figure 11 displays waveform data from the experiment in a cementitious mortar plate from Figure 5, $(d/\lambda \approx 1)$. The two dominant packets are attributed primarily to SH_0 and SH_1. In the present measurements, the dominant later packet is assigned primarily to SH_1 because it exhibits opposing phases between sensors 1 and 2 and has a slower group velocity than SH_0. This interpretation follows the previously published experimental method using vertically aligned receiving sensors, as mentioned in the methodology, where SH modes are identified from their relative arrival times and phase relationships. Dominant A_0 and S_0 contributions are considered unlikely: S_0 would be expected to travel substantially faster than SH_0, while A_0 would be expected to have a similar arrival region to the SH_1 packet but arrive in-phase. Although Lamb wave energy may be present due to the multimodal nature of the MPT excitation, the measured velocity and phase behaviour support the interpretation of this packet as SH dominated rather than purely SH.

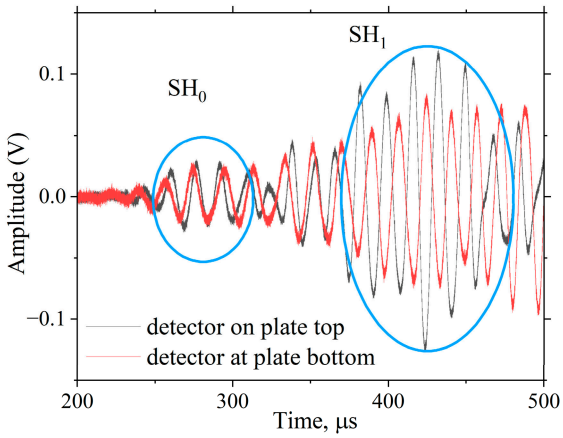


Figure 11. Waveform data from experiment on cementitious mortar plate, experiment setup Figure 5, with SH_0 and SH_1 modes circled for clarity.

3.4. Wave Modes in Cementitious Mortar Prisms Generated Using MPTs

Figure 12 shows that at 120 kHz ($d/\lambda \approx 4$), used in the COMSOL simulations of Figure 6, as the SH mode wavefront moves out of the mode formation zone, guided characteristics begin to appear. This wavefront out-of-plane directivity can be seen in the COMSOL simulation in Figure 12a. The COMSOL simulations in Figure 12 also reveal the launch angles on the SH generation components. SH packets radiate radially into the depth from the patch, reflecting off the bottom surface and spreading out. Most of the wave energy is launched into the bulk, reflecting off the bottom surface until higher order SH modes, in the case of the COMSOL simulation up to SH_6, are supported. Surface dwelling (surface-skimming bulk wave [36]) is also observed at the top of the prism.

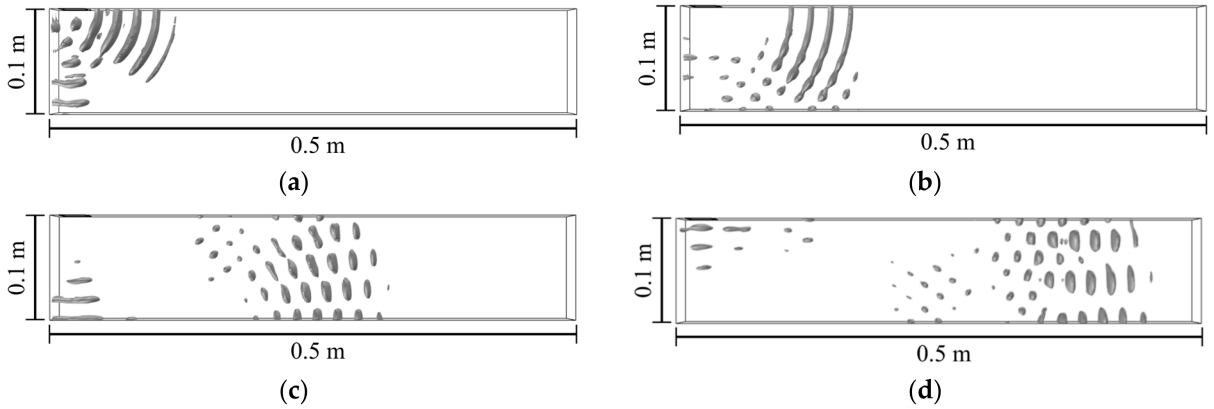


Figure 12. X (SH) energy within a 100 × 500 × 100 (mm^3) cementitious mortar prism, simulated in COMSOL, at times (**a**) 6.15 × 10^{-5} s; (**b**) 1.3 × 10^{-4} s; (**c**) 1.6 × 10^{-4} s; (**d**) 2.2 × 10^{-4} s. Greyscale colour legend was used as side-wall effects distorted side on visualisation, +1 m/s X-velocity shown in all figures.

The same COMSOL simulation is plotted using the XY-component of energy, the fundamental SV/Rayleigh displacement components. SV and Rayleigh waves become apparent, as shown in Figure 13, with Rayleigh waves travelling along the perimeter of the prism and around the edges, and SV quickly attenuating within the bulk.

Figure 14 displays a comparison between an out-of-plane piezoelectric sensor, and a racetrack-coil MPT sensor. A clear amplitude spike is seen on wave packet W_2 on the piezoelectric sensor. These findings validate out-of-plane motion on packet W_2 which is consistent with SV/Rayleigh motion.

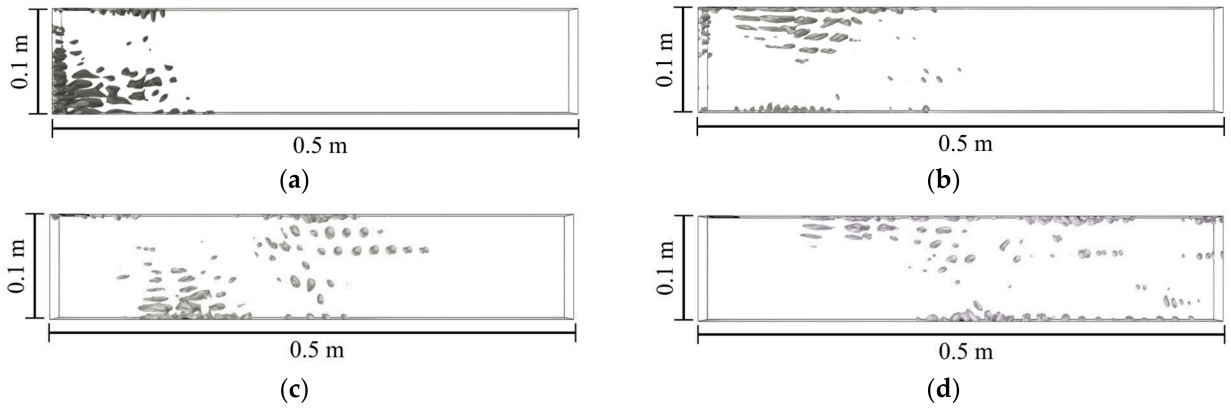


Figure 13. YZ (SV/Rayleigh) energy within a 100 × 500 × 100 (mm^3) cementitious mortar prism, simulated in COMSOL, at times 6.15×10^{-5} s (**a**), 1.3×10^{-4} s (**b**), 1.6×10^{-4} s (**c**), and 2.2×10^{-4} s (**d**). Greyscale colour legend was used as side-wall effects distorted side on visualisation, +1 m/s YZ-velocity shown in all figures.

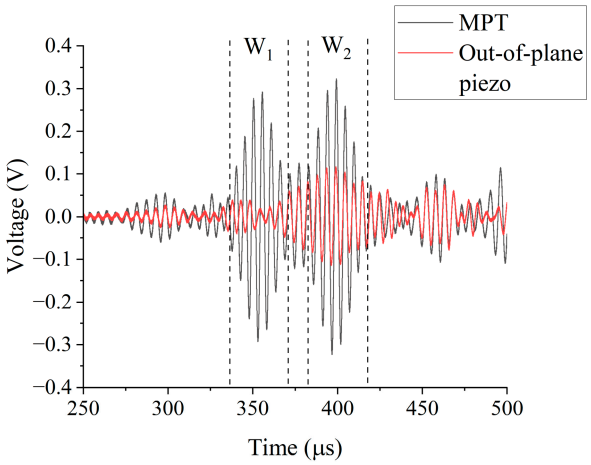


Figure 14. Waveform from both an out-of-plane piezoelectric receiver and MPT at equal distance from transducer on cementitious mortar prism seen in Figure 6b.

Using knowledge gained in previous experimentation Figure 6a,b it is possible to identify wave packets from the experimentation seen in Figure 6c. We can expect to see both SH and SV/Rayleigh packets supported with SH generated radially into the depth and on the surface with guided effects dependent on d/λ. SV/Rayleigh will include both SV and Rayleigh packets dependent on d/λ product, with SV quickly attenuating in the bulk.

Figure 15 and Table 3 show that when the MPTs are driven at 230 kHz $(d/\lambda) \approx 10$, seen in Figure 6c, the SH mode launches into the bulk radially, with its main lobe launched into the bulk at an angle which can be observed in the highest amplitude pulse seen at W_1 of 1-4. Since the generation is radial, surface-skimming SH dominates in the 1-2/1-4 sensor locations, though with less amplitude than the bulk launched wave.

SV modes in half-space media decay exponentially within an amount of surface depth which is theoretically derived from dispersion curves, and at this point can be defined as Rayleigh waves, though within the near field they hold their bulk-like launch energy enough to reach sensor 1-4 in bulk SV capacity. Other than 1-4, the SV modes are only found correctly after travelling along the surface of the prism, travelling around the perimeter of the prism on the bottom two (1-4, 1-5) sensors, consistent with Rayleigh and findings in [37]. Rayleigh/SV wave speeds are ∼80% of the SH speed, which is slower than the theoretical 88–95% of SH speed [31]. Rayleigh is a much more highly attenuated wave

mode when compared to its SH counterpart, which can be observed in 1-2 and 1-3 where W_2 is much more attenuated than its W_1 counterpart.

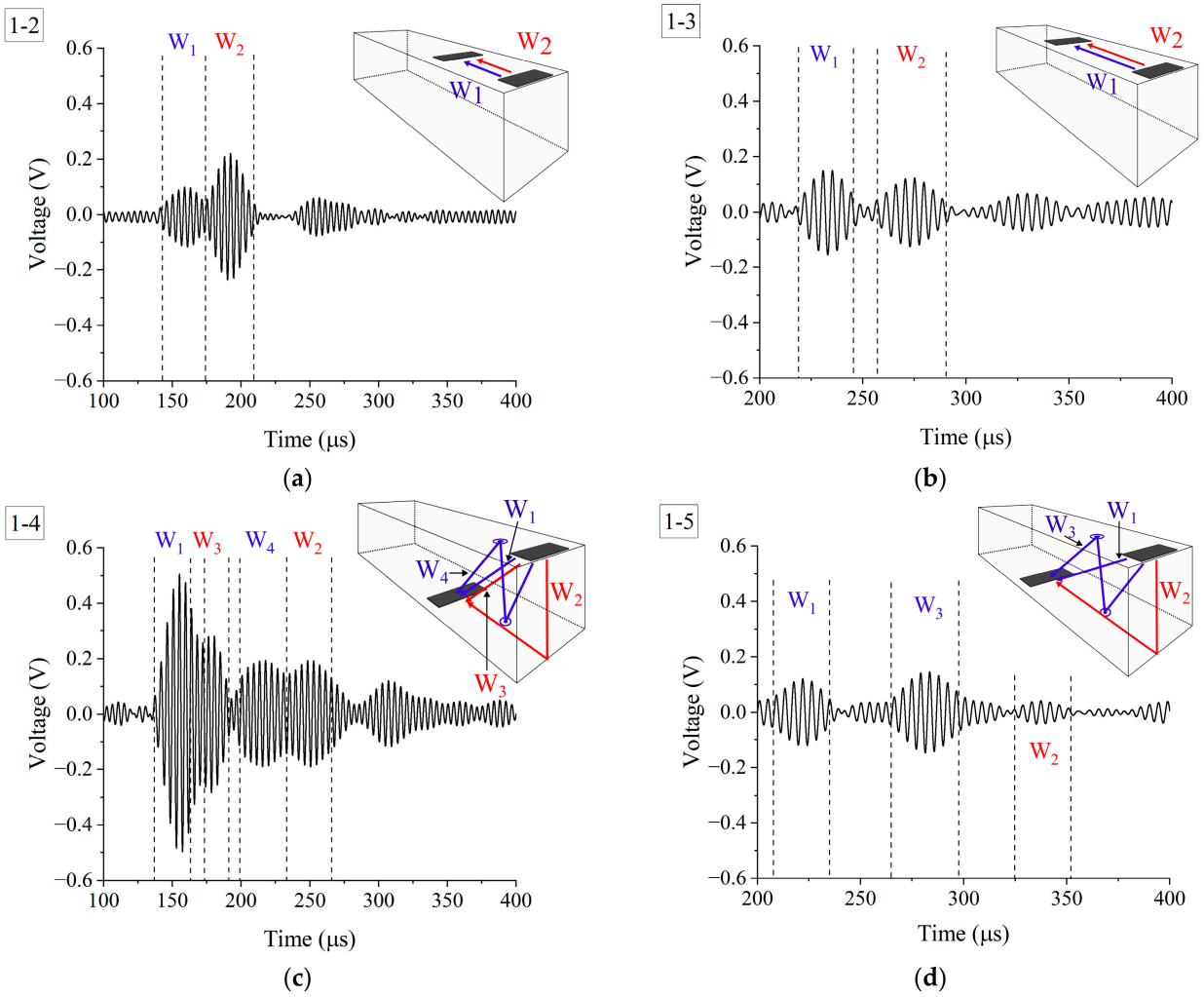


Figure 15. Waveform data and associated wave packet paths for 100 × 500 × 100 (mm^3) cementitious mortar prism experiment, seen in Figure 6c, for transducer-sensor pairs: (**a**) 1-2; (**b**) 1-3; (**c**) 1-4; (**d**) 1-5. W_n indicates assignment of different wave packets based on the wave speeds (Table 3). Blue indicates SH mode, red indicates SV/Rayleigh mode. Blue arrows indicate relative SH propagation paths, and red arrows indicate Rayleigh propagation paths.

Due to multimodal wavefield, the measured response contains overlapping SH, SV/Rayleigh, and reflected components, producing mode mixing, packet broadening, and local waveform distortion. Arrival times were therefore extracted from consistent, identifiable waveform features across comparable traces. The reported velocities are consequently treated as feature-based apparent velocities for modal assignment and relative comparison, rather than exact material wave speeds. The uncertainty shown in Table 3 includes sampling-time and probe-position resolution only; additional uncertainty from scattering, dispersion, and mode overlap is acknowledged.

Table 3. Identified wave speeds for wave packets observed from experiments on 100 × 500 × 100 (mm^3) cementitious mortar prism seen in Figure 15. Classification: Straight—a direct path (for sensors 1-2 and 1-3 this indicates the wave stays along the top surface); Perimeter—path around the perimeter of the cementitious mortar prism; reflected—indicates a number of reflections within the cementitious mortar prism from the top and bottom surface. Wave speed errors are calculated using standard uncertainty propagation, with $\sigma_c = c\frac{d}{t}\sqrt{(\sigma_d/d)^2 + (\sigma_t/t)^2}$ taking $\sigma_d = 0.01$ m and $\sigma_t = 2/230{,}000$ s (two-cycle picking uncertainty at 230 kHz).

Sensor	Waveform Label (W_n)	Wave Speed (m/s)	Wave Speed Error (±m/s)	Path	Mode Identification
1-2	1	1923	182.8	Straight	SH *
1-2	2	1458	114.8	Straight	Rayleigh
1-3	1	1837	106.5	Straight	SH *
1-3	2	1498	75.69	Straight	Rayleigh
1-4	1	1980	172.8	Straight	SH
1-4	2	1424	74.31	Perimeter	Rayleigh
1-4	3	1526	111.1	Straight	SV
1-4	4	2050	115.3	$Reflected_3$	SH
1-5	1	1960	113.9	Straight	SH
1-5	2	1506	58.39	Perimeter	Rayleigh

* Surface-skimming bulk wave.

3.5. Defect Detection in Cementitious Mortar Blocks

Figure 16 displays two waveforms exhibiting opposite sensitivities to defect location. Expressed relative to wavelength ($\lambda_{SH} \approx 12$ mm), the prism is ($d/\lambda \approx 12$), the flat-bottom holes extend to a depth of 70 mm (d/λ) ≈ 6, providing a strong scattering/attenuation feature. In the 2-2 experiment, the Rayleigh packet is well supported, while the SH contains a mix of the surface-skimming energy and that scattered from the subsurface defect bulk SH interference. Conversely, in the 1-1 experiment, the only well-supported packet is the bulk propagating SH, that reflects from the bottom of the prism, avoiding the defects. The SH and Rayleigh are largely attenuated by the hole defects.

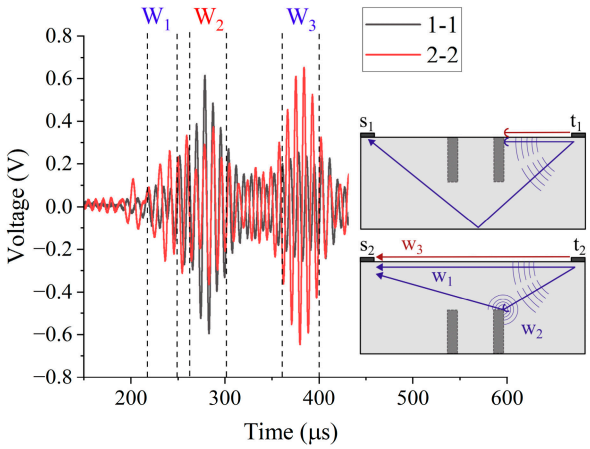


Figure 16. Waveforms from the defected cementitious mortar block test (setup in Figure 7). Trace 1-1: transducer–sensor pair on face of the defect. Trace 2-2: transducer–sensor pair on the opposite defect face. Propagation paths are illustrated with $W_{1,2}$ indicating SH arrivals, and W_3 indicating the SV/Rayleigh arrival. Blue arrows indicate relative SH propagation paths, and red arrows indicate Rayleigh propagation paths.

3.6. Tests on Fibre-Reinforced Concrete Prisms

At an excitation frequency of 80 kHz in a 150 mm thick fibre-reinforced concrete specimen, measured velocities were approximately 2200–2400 m/s for SH waves and 2000–2150 m/s for Rayleigh waves, as seen in Figure 17a. Across the five samples, the

mean peak flexural load was 11.57 kN, with a standard deviation of 0.96 kN and a coefficient of variation of 8.3%. The corresponding Side 1 MPT-measured SH wave speeds had a mean value of 2303 m/s, a standard deviation of 75.9 m/s, and a coefficient of variation of 3.3%.

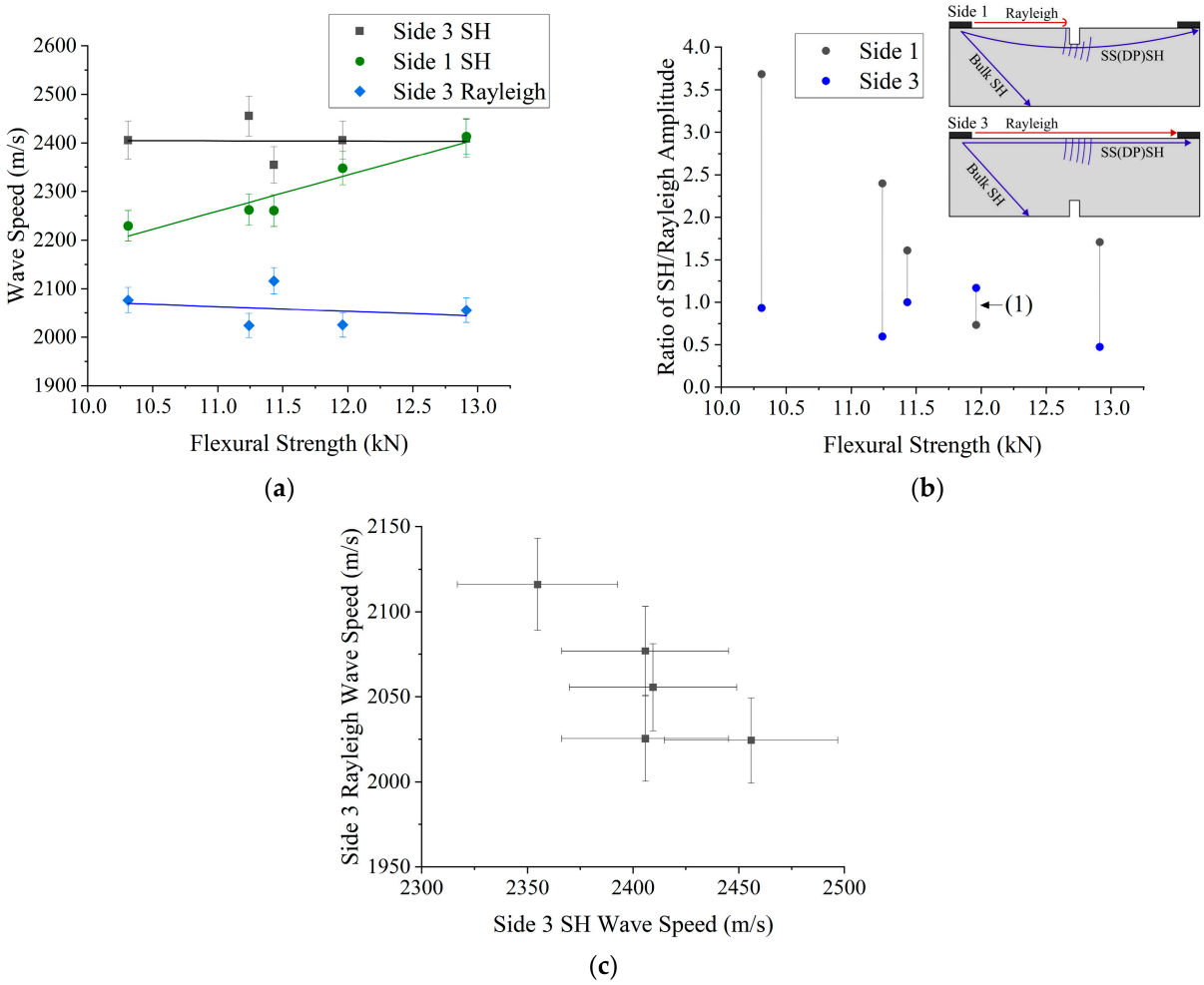


Figure 17. (**a**) Side 3 SH wave speed (m/s), Side 1 wave speed (m/s), and Side 3 Rayleigh wave speed (m/s) as a function of strength (kN) on first failure. Error bars show the wave speed uncertainty for $v = d/t$, computed as $\sigma_c = \frac{d}{t}\sqrt{\left(\frac{\sigma_d}{d}\right)^2 + \left(\frac{\sigma_t}{t}\right)^2}$ with $d = 0.65 \pm 0.005$ m (patch placement error) and $\sigma_t = 0.0625$ µs arrival-time picking uncertainty. Lines serve as guides to the eye; (**b**) SH/Rayleigh peak-to-peak amplitude for Side 1 and Side 3 with inset diagrams of wavefield propagation paths; (**c**) Side 3 Rayleigh against Side 3 SH speed, error bars show wave speed uncertainty from Figure 17a with outlier labelled as (1). All SH data is obtained from the first arriving surface-skimming shear horizontal (SSSH) packet.

From the mode generation study on racetrack-coil MPTs and finding the respective wavelengths of SH ($\lambda = c/f = \frac{2400}{80{,}000} = 30$ mm) and Rayleigh ($\lambda = c/f = \frac{2150}{80{,}000} = 27$ mm) modes, generation should be consistent with strong SH and SV/Rayleigh excitation at $(d/\lambda) \approx 5$.

Side 1′s SH wave speed increases (2230→2410 m/s) with flexural strength (10.31→12.91 kN). Comparing Side 3 and Side 1 measurements of wave speed in Figure 17a, general reduction in wave speed is noted. Side 3′s SH and Rayleigh speeds show no correlation with flexural strength as seen in Figure 17a. Figure 17c displays SH vs. Rayleigh speed for Side 3, while SH/Rayleigh speed ratio remains within theoretical limits for all samples (0.85–0.9), Rayleigh speed appears to decrease with increased SH speed on Side 3.

Results could not be plotted for Side 1's Rayleigh wave amplitude due to large attenuation of the wave packet and subsequent unreliability of choosing the correct arrival time. Instead, peak-to-peak voltage can be found for both SH and Rayleigh packets on both tested sides, as shown in Figure 17b as a ratio of SH/Rayleigh amplitude. Clear reductions in the SH/Rayleigh ratio are seen in the Side 3 results due to large Rayleigh attenuation on Side 1. Labelled (1) shows an outlier to this observation, poor adhesion between the sample and MPT was noted during experimentation, explaining the low SH amplitude on this reading.

4. Discussion

4.1. Patch Deformation

By using COMSOL simulation data, which was validated using LDV, the deformation of a racetrack-coil MPTs patch is found to largely follow the main magnetisation vectors from the bias and AC magnetic fields in the X and Y axis, while Z axis deformation is more dependent on material strain from the XY deformation components. This indicates that fast MPT prototyping can be performed using magnetisation vectors calculated in COMSOL. Subsequently the results presented in Figure 9 were used to construct the equivalent force model for COMSOL ultrasonic simulations of the generated wave modes. While other authors have used LDV [13] and finite element analysis [2,20] to model magnetostrictive deformation of MPTs, they have not yet been studied for racetrack-coil MPTs.

4.2. Modal Generation

Results from the modal generation study in Figure 10a,b show both SH_0 and A_0 are generated in glass plates by racetrack-coil MPTs, with mode-selective tuning available via frequency alteration. SH_0 generation is most efficient when the patch width (Y) is matched to the SH_0 wavelength. A_0 generation is most efficient when the patch width (Y) is slightly below the A_0 wavelength. Primary magnetisation vectors occur on the X (biassing magnets) and Y (AC coil field) directions, leading to deformation predominantly aligned with these in-plane magnetisation vectors as seen in Figure 2b. Accordingly magnetic domain rotation and magnetostrictive strain follow the imposed field directions. Out-of-plane (Z) deformation is not directly driven by a primary Z-oriented field but emerges through the constitutive magnetostrictive coupling used in the strain modules. The in-plane magnetostrictive strains (ε_{xx}, ε_{yy}, and associated shear terms) generate an accompanying ε_{zz} response through the material's magnetoelastic relations (and elastic compatibility/Poisson coupling), producing a secondary Z-displacement field. In practice this appears as a characteristic "rippling" of the surface, where Z-motion is a coupled consequence of the spatially varying XY strain field rather than an independently excited *Z*-axis actuation. This Z-deformation, paired with the Y-deformation, generates the SV/Rayleigh modes. Similar multimodal behaviour is reported by authors on different MPT configurations in [2,3,13].

4.3. Multimodal Generation in Cementitious Mortar Prisms

Both SH and SV/Rayleigh modes have been produced by racetrack-coil MPTs in cementitious mortar. In the $100 \times 500 \times 100$ (mm^3) prism, the observed Rayleigh/SV packet speed was markedly lower than expected ($\approx 0.80\ c_{SH}$, Table 3), whereas in fibre-reinforced concrete the Rayleigh ratio is closer to theoretical expectations ($\approx 0.88\ c_{SH}$). While the Rayleigh–shear velocity ratio depends on Poisson's ratio (ν), isotropic half-space theory predicts Rayleigh speed only slightly below shear speed (typically $\sim 0.87 - 0.95\ c_{SH}$), so a reduction to $\sim 0.80\ c_{SH}$ is unlikely to be explained by ν alone and instead suggests a lowered apparent velocity likely due to: lingering guided wave effects, near-field/formation effects at short stand-off (Fresnel region), propagation in a lower-velocity near-surface layer (lai-

tance, microcracking, carbonation, porosity/moisture gradients), and/or mode mixing in a heterogeneous block where the labelled SV/Rayleigh packet contains surface-guided/leaky components [37]. Guided-wave and dispersion theory still applies for higher-order modes in cementitious mortar as shown in the COMSOL simulations of Figure 12 where SH_6 is supported, and the cementitious mortar plate study of Figure 11 where SH_1 is supported. In short pitch-catch experimentation mode mixing interference during the mode formation zone will cause difficulty in identifying significant data, as reported by other authors [35,38]. In half-space cementitious mortar, the radial generation into the depth by racetrack-coil MPTs presents both bulk SH and surface-skimming SH. Application of this is examined in the following discussion.

Practical deployment of MPTs on concrete introduces several sources of uncertainty that were not fully isolated in the present study. In real structural members concrete heterogeneity arising from coarse aggregates, pores, and interfacial transition zones can perturb the coherent wavefield, alter apparent phase/group velocities, and increase attenuation, particularly at higher frequencies where wavelengths become shorter and multiple scattering becomes more significant [39,40]. Environmental conditions may also affect inspection accuracy, as moisture content, saturation gradients and temperature variations can modify ultrasonic velocity, attenuation and effective elastic properties [41]. Therefore, the excitation wavelength should be selected to be larger than the characteristic aggregate size to reduce scattering effects and improve the stability of the measured wavefield.

Although tape-mounted MPTs produced repeatable signals in the present experiments, adhesive coupling should be considered a potential source of amplitude variability. For SH wave generation, in-plane shear traction must be transmitted across the patch–adhesive–substrate interface, so local changes in tape thickness, incomplete contact, air gaps, or surface roughness may alter the transferred shear force. Wen et al. modelled this effect using an interface parameter based on bonding layer stiffness and thickness, showing that bonding conditions affect generated SH wave amplitude but not the optimal excitation frequency [42]. Similarly, Sha et al. reported that adhesive stiffness and thickness influence the amplitude response of MPTs [3]. Therefore, while double-sided tape was suitable for removable, non-destructive MPT placement in this low-frequency study, coupling efficiency was not independently quantified and may have contributed to variations in measured signal amplitude.

Future work should incorporate heterogeneous modelling, random aggregate realisations, environmental monitoring and calibration procedures, as well as a parametric study of adhesive type, adhesive thickness, surface preparation, applied pressure, epoxy bonding and gel-assisted coupling, to improve reliability under practical deployment conditions. Future work should also use denser spatial scanning and larger propagation apertures to enable more robust wavenumber–frequency, wavelet-based, or modal-decomposition analysis of the overlapping wave packets.

4.4. Fibre-Reinforced Prisms

Results from the fibre-reinforced concrete prism tests show a correlation between the surface-skimming SH wave speed and the peak load measured during the 3-point bend test. In particular, the SH wave speed measured on the loaded/notched side of the prism, Side 1 as shown in Figure 8a, increases with the measured strength, as shown in Figure 17a. The prisms were nominally identical, with the main expected source of strength variation being local variation in material constituents, including steel fibres and coarse aggregate, around the Side 1 notch and breaking region. This provides a plausible explanation for why the wave-speed change is observed more clearly on Side 1 than on Side 3. Unlike conventional reinforcement bars, randomly distributed steel

fibres can contribute to the tensile and flexural response of the cementitious matrix by bridging cracks, delaying crack growth, and sustaining load after initial cracking [43]. Therefore, a plausible mechanism for the observed strength increase is a locally stiffer tensile/flexural zone caused by a higher effective fibre content and/or more favourable fibre orientation near the peak-stress region. Since SH wave speed is governed by the effective shear modulus and density of the interrogated material, this local stiffness increase would be expected to increase the measured SH wave speed. Density increases within the loaded/tensile region are expected to be modest for steel-fibre addition. Using approximate densities $\left(\rho_{concrete} \approx 2400\ \mathrm{kgm}^{-3},\ \rho_{steel} \approx 7800\ \mathrm{kgm}^{-3}\right)$ the density ratio is estimated here as $1.02 \lesssim \rho_2/\rho_1 \lesssim 1.05$. Using the SH wave speed equation from Table 2:

$$c_{SH} = \sqrt{\frac{G}{\rho}} \ \Rightarrow\ G = \rho c_{SH}^2,$$

the effective shear modulus ratio follows as:

$$\frac{G_2}{G_1} = \frac{\rho_2}{\rho_1}\left(\frac{c_2}{c_1}\right)^2.$$

Taking a conservative upper bound $\rho_2/\rho_1 = 1.05$ and measured SH speeds $c_1 = 2230$ m/s and $c_2 = 2410$ m/s from results in Figure 17a gives:

$$\frac{G_2}{G_1} \approx 1.05\left(\frac{2410}{2230}\right)^2 \approx 1.23,$$

i.e., an ~23% increase in effective shear modulus. In comparison, the 3-point bend peak load increases from $P_1 = 10.31$ kN to $P_2 = 12.91$ kN implying a proportional increase in strength capacity:

$$\frac{P_2}{P_1} = \frac{12.91}{10.31} = 1.25,$$

i.e., ~25%. The close agreement between the shear-modulus increase inferred from the SH speed, ~23%, and the measured increase in peak flexural load, ~25%, suggests that the SH wave speed measurement is sensitive to the same fibre-driven mechanical changes that influence the strength response.

However, this comparison should be interpreted cautiously. The 3-point bend test provides a global mechanical response governed by crack initiation, crack bridging, fibre pull-out, matrix strength, aggregate distribution, fibre orientation, and the local fracture process zone. In addition, local variation in coarse-aggregate distribution may also influence the measured ultrasonic velocity by altering the effective stiffness, density, scattering behaviour, and propagation path within the interrogated region. By contrast, the MPT measurement is governed by the local effective material properties along the ultrasonic propagation path. A more direct validation would require correlation between locally estimated shear modulus, local fibre volume fraction, fibre orientation, aggregate distribution, and the microstructure of the fibre–matrix/interface transition zones.

Similar observations have been reported on non-fibre-reinforced samples by other authors where longitudinal [44] and SH [45] wave velocity was used to predict compressive-strength, but equivalent SH-wave-based correlations in fibre-reinforced concrete remain limited. This interpretation also aligns with prior flexural studies of steel-fibre concrete and steel-fibre lightweight concrete, which consistently attribute flexural-strength gains to fibre crack-bridging that delays crack initiation and sustains load after first cracking [46].

As illustrated in Figure 18, the effective shear modulus governing SH/SV/Rayleigh wave speed is expected to be most sensitive to an increased population of fibres aligned

predominantly within the Y-plane, with minimal XZ components, as observed by other authors in [47], where fibre-orientation was found to be consistent with tensile-strength using AC-IS. This preferential alignment acts as an anisotropic contributor to the bulk shear response, and the same orientation would be expected to most effectively enhance both flexural- and tensile-strength. Consequently, transverse waves may provide a more direct indicator of fibre-reinforced concrete flexural- and tensile-strength than longitudinal waves. Notably, increases in bulk density and shear modulus should not scale proportionally: density increases reflect the total fibre content across all orientations, whereas the effective shear modulus is governed by the local fibre orientation distribution and spatial concentration within the interrogated volume. For a random fibre field, density may therefore increase more rapidly than the shear-modulus-driven wave-speed increase, particularly if the fraction of favourably oriented fibres does not rise at the same rate as the total fibre content.

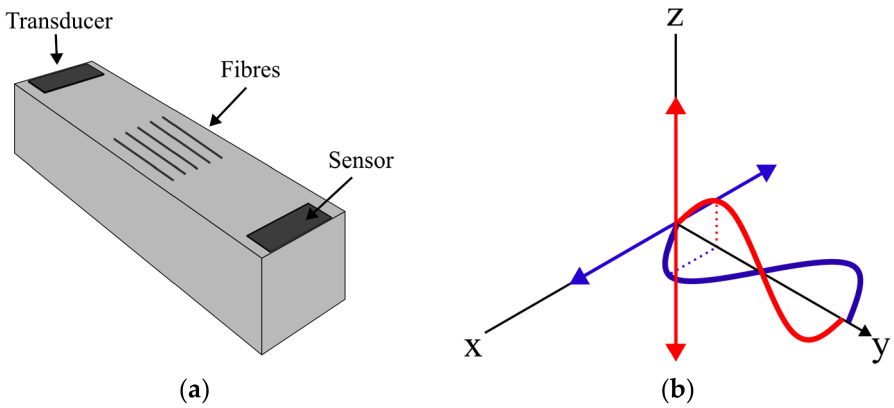


Figure 18. (**a**) Ideal fibre orientation in fibre-reinforced concrete to increase shear modulus and flexural- and tensile-strength during a 3-point bend test; (**b**) diagram with blue arrow indicating SH wave motion and blue sinusoidal trace indicating the propagating wave (X), red arrow indicating SV/Rayleigh wave motion and red sinusoidal trace indicating the propagating wave (Z), and direction of propagation (Y).

At wavelength ≈ 30 mm the fibres (typ. 0.5–1.0 mm diameter, 25–60 mm length) [48] are sub-wavelength features. Equivalent-medium theory suggests they are not individually resolved by the propagating field and should contribute limited fibre-scale scattering. The prism is therefore treated as a bulk-averaged medium at this scale, meaning fibre scattering is unlikely to be the dominant cause of packet distortion or apparent wave-speed shifts. Instead, changes are again more plausibly attributed to bulk-averaged material properties, particularly the effective shear modulus entering the SH wave speed relation.

Importantly, Rayleigh speeds could not be gathered from Side 1 due to the notch largely blocking Rayleigh propagation, simulated in Figure 19, demonstrating a use case for multimodal testing in situations where defects obstruct one mode but allow another. Figure 17c highlights the influence of propagation depth sensitivity. Contrary to the theoretical behaviour expected in isotropic media, Rayleigh wave speed does not increase alongside the SH wave speed. A likely explanation is that Rayleigh waves, owing to their shallower penetration depth, are less directly governed by the same bulk shear properties as deeper penetrating SH waves. Instead, heterogeneity in the fibre-reinforcement distribution may have led to different effective shear moduli along the respective propagation paths, and corresponding deviated wave speeds. Due to notch-induced attenuation Rayleigh wave measurements on Side 1 were not obtainable; therefore, the effectiveness of using this behaviour to predict fibre-reinforcement density near the peak stress region cannot be assessed.

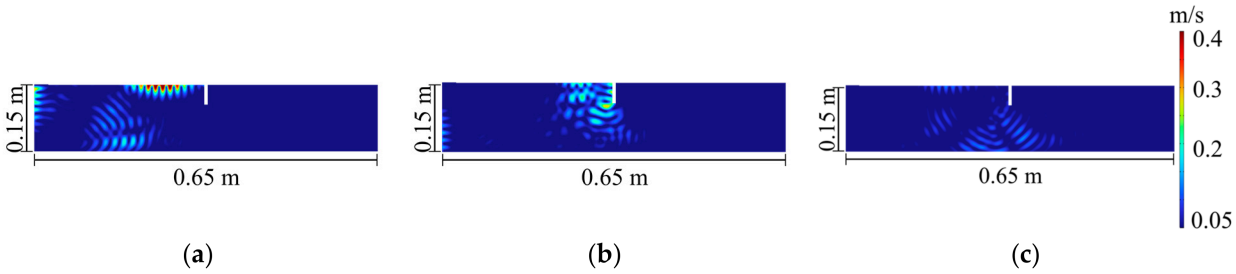


Figure 19. COMSOL 2D elastic waves simulation on a 150 × 650 (mm^2) concrete sample, showing SV/Rayleigh wave velocity magnitude and notch root scattering at times: (**a**) 1.3×10^{-4}; (**b**) 1.8×10^{-4}; (**c**) 2.1×10^{-4}.

4.5. Interplay of Defects and Wave Modes in Cementitious Media

Results from the fibre-reinforced and flat-bottom-hole studies demonstrate that a single racetrack-coil MPT can exploit both SH and Rayleigh components for defect detection. Rayleigh waves show the highest sensitivity to near-surface damage (approximately within one wavelength in depth), whereas SH energy partitions between a surface-skimming component and a bulk component that can interact with deeper defects depending on defect depth, face, and the thickness–wavelength regime.

In the flat-bottom-hole tests (Figure 16), the dominant change is observed in the SH response, the bulk SH wavefront interacts with defects located on the opposite face to the transducer–sensor pair, producing strong amplitude reduction and waveform distortion consistent with destructive interference relative to the surface-skimming packet. Conversely, in the fibre-reinforced concrete tests, the notch defect does not extend sufficiently deep to fully obstruct either SH path, though interference is observed at the beginning of the surface-skimming packet. These observations strongly indicate MPTs can be useful for defect detection across multiple regimes in cementitious media; however, since the generated wavefield behaviour is strongly dependent on specimen geometry, the thickness–to-wavelength ratio, and defect geometry and location, more work is needed to quantify the complex relationship, possibly through the use of machine learning, with extended regime-based datasets.

5. Conclusions

This paper presents a combined modelling and experimental framework for analysing racetrack-coil MPT ultrasonic wavefield behaviour in cementitious media, fibre-reinforced concrete, and glass. Key outcomes are:

We validated a MPT magnetostriction COMSOL model using LDV. As expected, the patch deformation affects wave mode generation and can be tuned via frequency to mainly generate either SH or SV/Rayleigh modes. The model was then used to predict and untangle multiple modes generated in cementitious mortar prisms.

We demonstrated for the first time the generation and detection of SH-guided waves in 30 mm thick cementitious mortar plates, identifying SH_0 and SH_1 modes.

In cementitious mortar prisms (in the quasi-plate/half-space regime) Rayleigh-type modes are generated from racetrack-coil MPTs, however in short pitch–catch measurements the apparent Rayleigh speed is lower than expected, likely due to near-field/formation effects, lingering guided-wave behaviour, heterogeneity, and free-surface interactions. Despite this, SH and the Rayleigh-dominated packets remain sufficiently distinct for reliable picking and analysis.

Rayleigh waves are more sensitive to surface-breaking damage, such as perpendicular cuts or flat-bottom holes, while surface-skimming SH waves propagate around such surface defects, preserving useful information about the underlying material and enabling assess-

ment even when the inspected surface is damaged. Additionally, bulk SH waves launched at an angle can probe interior properties of cementitious media, though their identification is more complex due to multiple reflections between the top and bottom surfaces.

In steel fibre-reinforced concrete, SH wave speed correlated with breaking strength. The increase in breaking strength is influenced by the fibre distribution and orientation near the region of maximum stress, while the absolute strength also depends on the concrete matrix properties. In systems with random fibre distribution, this heterogeneity affects all measured wave speeds, including traditionally used bulk shear and bulk compressive waves. However, the local near-surface resistance to breaking can be probed most sensitively by surface-skimming SH waves (which are effectively generated with MPTs) due to fibre-wave orientation.

These results indicate MPTs can be useful tools for NDE in cementitious media. Using multimodal testing, defect characterisation and material properties can be explored more effectively than singular mode testing, if the waveforms can be examined efficiently enough to decipher packet identification and meaning.

Future work will look to expand the field of MPT testing with cementitious media utilising both SH and Rayleigh modes to gain insights into difficult material categorisation and defect identification through comparisons between the modes, possibly using machine learning to aid the difficult mode identification and analysis process. Future work could also look to exploit MPTs' major advantages, their non-contact excitation and flexibility, possibly through embedding sensors or creating new MPT configurations to gain specific insights per MPT.

Author Contributions: Conceptualization, Z.L.W. and O.T.; methodology, Z.L.W. and O.T.; software, Z.L.W.; validation, Z.L.W.; formal analysis, Z.L.W.; investigation, Z.L.W., O.T., S.K., S.A. (Saida Alimdjanova), R.Y., S.A. (Sadiq Abdullahi) and L.M.; fibre-reinforced concrete samples, R.Y. and L.M.; resources, O.T., R.Y. and L.M.; data curation, Z.L.W. and S.K.; writing—original draft preparation, Z.L.W.; writing—review and editing, Z.L.W., O.T. and D.B.; visualisation, Z.L.W.; supervision, O.T. and D.B.; project administration, O.T. and D.B.; funding acquisition, O.T. All authors have read and agreed to the published version of the manuscript.

Funding: This research was funded by Royal Society, grant number (RG/R1/241449).

Data Availability Statement: Data is available on request.

Acknowledgments: The authors thank Building Research Establishment group (BRE) for support in destructive testing of fibre-reinforced concrete and for assistance in making the samples.

Conflicts of Interest: Authors L. Marston and S. Abdullahi were employed by the company Fibretech Ltd. Author R. Young was employed by the company Lateral Logic Ltd. The remaining authors declare that the research was conducted in the absence of any commercial or financial relationships that could be construed as a potential conflict of interest.

Abbreviations

The following abbreviations are used in this manuscript:

MPT	Magnetostrictive patch transducer
NDE	Non-destructive evaluation
SHM	Structural health monitoring
SH	Shear-horizontal
SV	Shear-vertical
LDV	Laser-Doppler vibrometry

References

1. Wang, S.; Li, C.; He, C.; Ma, X.; Zhai, G. Design method of unidirectional wideband SH guided wave phased array magnetostrictive patch transducer. *Sens. Actuators A Phys.* **2022**, *344*, 113710. [CrossRef]
2. Kim, Y.Y.; Kwon, Y.E. Review of magnetostrictive patch transducers and applications in ultrasonic nondestructive testing of waveguides. *Ultrasonics* **2015**, *62*, 3–19. [CrossRef] [PubMed]
3. Sha, G.; Lissenden, C.J. Modeling Magnetostrictive Transducers for Structural Health Monitoring: Ultrasonic Guided Wave Generation and Reception. *Sensors* **2021**, *21*, 7971. [CrossRef] [PubMed]
4. Malyugin, D.V. On the theory of Wiedemann effects. *J. Magn. Magn. Mater.* **1991**, *97*, 193–197. [CrossRef]
5. Dapino, M.J. On magnetostrictive materials and their use in adaptive structures. *Struct. Eng. Mech.* **2004**, *17*, 303–329. [CrossRef]
6. Vinogradov, S.; Cobb, A.; Fisher, J. New Magnetostrictive Transducer Designs for Emerging Application Areas of NDE. *Materials* **2018**, *11*, 755. [CrossRef] [PubMed]
7. Liu, Z.; Zhang, Y.; Xie, M.; Li, A.; Bin, W.; He, C. A direction-tunable shear horizontal mode array magnetostrictive patch transducer. *NDT E Int.* **2018**, *97*, 20–31. [CrossRef]
8. Lee, J.S.; Kim, Y.Y.; Cho, S.H. Beam-focused shear-horizontal wave generation in a plate by a circular magnetostrictive patch transducer employing a planar solenoid array. *Smart Mater. Struct.* **2009**, *18*, 015009. [CrossRef]
9. Yoo, B.; Na, S.M.; Flatau, A.B.; Pines, D.J. Directional magnetostrictive patch transducer based on Galfenol's anisotropic magnetostriction feature. *Smart Mater. Struct.* **2014**, *23*, 095035. [CrossRef]
10. Hou, E.Z.Y.; Rostami, J.; Li, G.G.D.; Huang, G. Performance investigation on the balance of static and dynamic magnetic field strength of magnetostrictive patch transducer with different permanent magnets. *J. Instrum.* **2022**, *17*, P05007. [CrossRef]
11. Wu, J.; Tang, Z.; Yang, K.; Lv, F. Signal strength enhancement of magnetostrictive patch transducers for guidedwave inspection by magnetic circuit optimization. *Appl. Sci.* **2019**, *9*, 1477. [CrossRef]
12. Xie, C.; Liu, T.; Pei, C.; Chen, Z. A Flexible Thin-Film Magnetostrictive Patch Guided-Wave Transducer for Structural Health Monitoring. *IEEE Sens. J.* **2022**, *22*, 12237–12244. [CrossRef]
13. Zitoun, A.; Dixon, S.; Edwards, G.; Hutchins, D. Experimental study of the guided wave directivity patterns of thin removable magnetostrictive patches. *Sensors* **2020**, *20*, 7189. [CrossRef] [PubMed]
14. Cousin, G.; Lhémery, A.; Grondel, S. A model to predict the elastic field radiated by a magnetostrictive patch transducer into an omnidirectional waveguide. *J. Phys. Conf. Ser.* **2021**, *1761*, 012005. [CrossRef]
15. Oh, J.H.; Sun, K.H.; Kim, Y.Y. Time-harmonic finite element analysis of guided waves generated by magnetostrictive patch transducers. *Smart Mater. Struct.* **2013**, *22*, 85007. [CrossRef]
16. Kim, H.J.; Lee, J.S.; Kim, H.W.; Lee, H.S.; Kim, Y.Y. Numerical simulation of guided waves using equivalent source model of magnetostrictive patch transducers. *Smart Mater. Struct.* **2015**, *24*, 015006. [CrossRef]
17. Wang, S.; Liang, Q.; Li, C.; Li, Z.; Li, Y. Design of guided wave magnetostrictive patch transducer with vertical static bias magnetic field for pipe inspection. *Sens. Actuators A Phys.* **2024**, *376*, 115611. [CrossRef]
18. Gao, W.; Zhang, D.; Zhang, E.; Yan, X. Noncontact Magnetostrictive Torsional Guided Wave Sensors for Small-Diameter Pipes. *IEEE Trans. Instrum. Meas.* **2021**, *70*, 6002709. [CrossRef]
19. Cao, S.; Li, M.M.; Wang, Q.; Weng, L.; Huang, W.M. Torsional mode magnetostrictive patch transducer with TPSMs for liquid-filled pipes inspection. *AIP Adv.* **2023**, *13*, 035308. [CrossRef]
20. Zitoun, A.; Dixon, S.; Kazilas, M.; Hutchins, D. The Effect of Changes in Magnetic Field and Frequency on the Vibration of a Thin Magnetostrictive Patch as a Tool for Generating Guided Ultrasonic Waves. *Sensors* **2022**, *22*, 766. [CrossRef] [PubMed]
21. Miao, H.; Li, F. Shear horizontal wave transducers for structural health monitoring and nondestructive testing: A review. *Ultrasonics* **2021**, *114*, 106355. [CrossRef] [PubMed]
22. Zheng, W.; Qi, C.; Tian, J.; Zhao, W.; Su, Y.; Feng, Z. Research on ultrasonic visualization of defects in reinforced concrete beams based on amplitude method. In *Proceedings of the Fourth International Conference on Sensors and Information Technology (ICSI 2024)*; SPIE: Bellingham, WA, USA, 2024; p. 152. [CrossRef]
23. Xu, X.; Ran, B.; Jiang, N.; Xu, L.; Huan, P.; Zhang, X.; Li, Z. A systematic review of ultrasonic techniques for defects detection in construction and building materials. *Measurement* **2024**, *226*, 114181. [CrossRef]
24. Bompan, K.F.; Haach, V.G. Ultrasonic tests in the evaluation of the stress level in concrete prisms based on the acoustoelasticity. *Constr. Build. Mater.* **2018**, *162*, 740–750. [CrossRef]
25. Liu, J.; Zhao, M.; Wang, K.; Chen, Y.; Cheng, Y.; Fan, Z. Nonlinear ultrasonic testing of concrete damage based on the stress–strain relationship of concrete hysteresis in non-classical nonlinear models. *Appl. Acoust.* **2025**, *235*, 110691. [CrossRef]
26. Xue, Q.; Larose, E.; Moreau, L.; Thery, R.; Abraham, O.; Henault, J.-M. Ultrasonic monitoring of stress and cracks of the 1/3 scale mock-up of nuclear reactor concrete containment structure. *Struct. Health Monit.* **2021**, *21*, 1474–1482. [CrossRef]
27. Sbartaï, Z.M.; Garnier, V.; Villain, G.; Breysse, D. Assessment of Concrete by a Combination of Non-Destructive Techniques. In *Non-Destructive Testing and Evaluation of Civil Engineering Structures*; Elsevier: Amsterdam, The Netherlands, 2018; pp. 259–297. [CrossRef]

28. Darmon, M.; Khalid, N.; Ramaniraka, M.; Dorval, V.; Henault, J.M.; Chaix, J.F. Modeling of ultrasonic velocity and attenuation for concrete inspection: A review. *Ultrasonics* **2025**, *154*, 107690. [CrossRef] [PubMed]
29. Alqurashi, I.; Alver, N.; Bagci, U.; Catbas, F.N. A Review of Ultrasonic Testing and Evaluation Methods with Applications in Civil NDT/E. *J. Nondestruct. Eval.* **2025**, *44*, 53. [CrossRef]
30. Lee, S.; Popovics, J.S. Ultrasonic defect detection in a concrete slab assisted by physics-informed neural networks. *NDT E Int.* **2025**, *151*, 103311. [CrossRef]
31. Rose, J.L. *Ultrasonic Guided Waves in Solid Media*; Cambridge University Press: Cambridge, UK, 2014.
32. Cheeke, J.D.M. *Fundamentals and Applications of Ultrasonic Waves*; CRC Press: Boca Raton, FL, USA, 2017.
33. Trushkevych, O.; Dixon, S. Soft magnetostrictive patches for guided wave ultrasonics using Wiedemann effect-based MPTs and EMATs. *Insight Non-Destr. Test. Cond. Monit.* **2024**, *66*, 12–18. [CrossRef]
34. Cho, S.H.; Sun, K.H.; Lee, J.S.; Kim, Y.Y. Development of an Orientation-Adjustable Patch-Type Magnetostrictive Sensor for Damage Detection in a Plate. In Proceedings of the 16th World Conference on NDT—2004—Montreal (Canada), Montreal, QC, Canada, 30 August–3 September 2004; Available online: https://www.ndt.net/?id=2206 (accessed on 10 April 2026).
35. Kubrusly, A.C.; Freitas, M.A.; von der Weid, J.P.; Dixon, S. Mode Selectivity of SH Guided Waves by Dual Excitation and Reception Applied to Mode Conversion Analysis. *IEEE Trans. Ultrason. Ferroelectr. Freq. Control* **2018**, *65*, 1239–1249. [CrossRef] [PubMed]
36. Lewis, M. Surface Skimming Bulk Wave, SSBW. In *Proceedings of the 1977 Ultrasonics Symposium*; IEEE: New York, NY, USA, 1977; pp. 744–752. [CrossRef]
37. Benech, N.; Brum, J.; Grinspan, G.; Aguiar, S.; Negreira, C.A. Analysis of the transient surface wave propagation in soft-solid elastic plates. *J. Acoust. Soc. Am.* **2017**, *142*, 2919–2932. [CrossRef] [PubMed]
38. Petcher, P.A.; Dixon, S. Mode mixing in shear horizontal ultrasonic guided waves. *Nondestruct. Test. Eval.* **2017**, *32*, 113–132. [CrossRef]
39. Ramaniraka, M.; Rakotonarivo, S.; Payan, C.; Garnier, V. Effect of the Interfacial Transition Zone on ultrasonic wave attenuation and velocity in concrete. *Cem. Concr. Res.* **2019**, *124*, 105809. [CrossRef]
40. Knak, M.; Nitka, M.; Rucka, M. Discrete element method modelling of elastic wave propagation in a meso-scale model of concrete. *Ultrasonics* **2024**, *141*, 107336. [CrossRef] [PubMed]
41. Diewald, F.; Denolle, M.; Timothy, J.J.; Gehlen, C. Impact of temperature and relative humidity variations on coda waves in concrete. *Sci. Rep.* **2024**, *14*, 18861. [CrossRef] [PubMed]
42. Wen, F.; Shan, S.; Radecki, R.; Staszewski, W.J.; Cheng, L. Shear-lag modelling of surface-bonded magnetostrictive transducers for shear horizontal wave generation in a non-ferromagnetic plate. *Smart Mater. Struct.* **2021**, *30*, 035026. [CrossRef]
43. Park, S.H.; Kim, D.J.; Ryu, G.S.; Koh, K.T. Tensile behavior of Ultra High Performance Hybrid Fiber Reinforced Concrete. *Cem. Concr. Compos.* **2012**, *34*, 172–184. [CrossRef]
44. Sabbağ, N.; Uyanık, O. Prediction of reinforced concrete strength by ultrasonic velocities. *J. Appl. Geophys.* **2017**, *141*, 13–23. [CrossRef]
45. Lin, S.; Tang, X.; Li, H.-N.; Gucunski, N.; Wang, Y. Nondestructive Evaluation of Concrete Compressive Strength Using Shear-Horizontal Waves. *J. Perform. Constr. Facil.* **2023**, *37*, 06022002. [CrossRef]
46. Mohamed, A.M.; Tayeh, B.A.; Abu Aisheh, Y.I.; Salih, M.N.A. Exploring the performance of steel fiber reinforced lightweight concrete: A case study review. *Case Stud. Constr. Mater.* **2023**, *18*, e01968. [CrossRef]
47. Ozyurt, N.; Mason, T.O.; Shah, S.P. Non-destructive monitoring of fiber orientation using AC-IS: An industrial-scale application. *Cem. Concr. Res.* **2006**, *36*, 1653–1660. [CrossRef]
48. Pham, T.M. Fibre-reinforced concrete: State-of-the-art-review on bridging mechanism, mechanical properties, durability, and eco-economic analysis. *Case Stud. Constr. Mater.* **2025**, *22*, e04574. [CrossRef]

Disclaimer/Publisher's Note: The statements, opinions and data contained in all publications are solely those of the individual author(s) and contributor(s) and not of MDPI and/or the editor(s). MDPI and/or the editor(s) disclaim responsibility for any injury to people or property resulting from any ideas, methods, instructions or products referred to in the content.